nature materials

Article

https://doi.org/10.1038/s41563-022-01417-9

Granular aluminium nanojunction fluxonium qubit

In the format provided by the authors and unedited

Supplementary Information for Granular Aluminum Nano-Junction Fluxonium Qubit

D. Rieger,[1,*] S. Günzler,[1,2,†] M. Spiecker,[1] P. Paluch,[1,2] P. Winkel,[1,2] L. Hahn,[3] J. K. Hohmann,[3] A. Bacher,[3] W. Wernsdorfer,[1,2] and I. M. Pop[1,2,‡]

[1]*PHI, Karlsruhe Institute of Technology, 76131 Karlsruhe, Germany*
[2]*IQMT, Karlsruhe Institute of Technology, 76344 Eggenstein-Leopoldshafen, Germany*
[3]*IMT, Karlsruhe Institute of Technology, 76344 Eggenstein-Leopoldshafen, Germany*

(Dated: October 20, 2022)

CONTENTS

* dennis.rieger@kit.edu
† First two authors contributed equally.
‡ ioan.pop@kit.edu

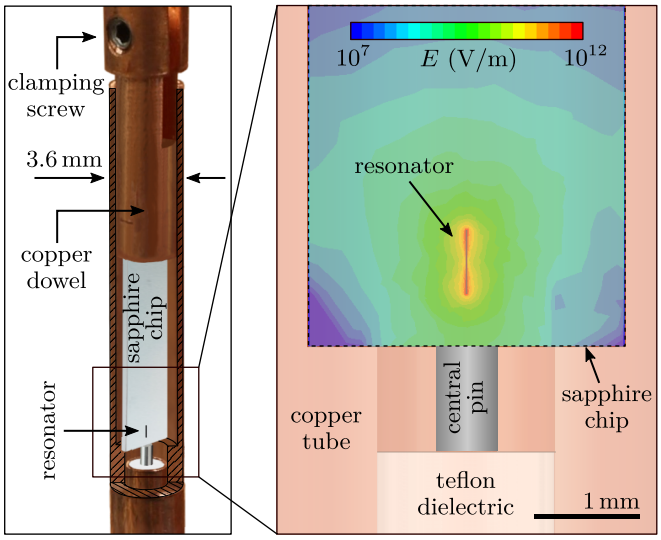

FIG. S1. **Cylindrical waveguide sample holder (left side) and color plot of a finite element simulation of the electric field distribution (right side).** The cylindrical waveguide design is the same we used in Ref. [1] to measure grAl resonators in magnetic fields up to 1 T. The sapphire chip is fixed by a copper dowel, which is tightened against the walls of the waveguide copper tube using the clamping screw. The readout resonator is located at a distance of about 0.5 mm from the bottom edge of the chip, close to the stripped central pin of a 2.2 mm coaxial cable with teflon dielectric. The electric field scale corresponds to an energy of 1 J.

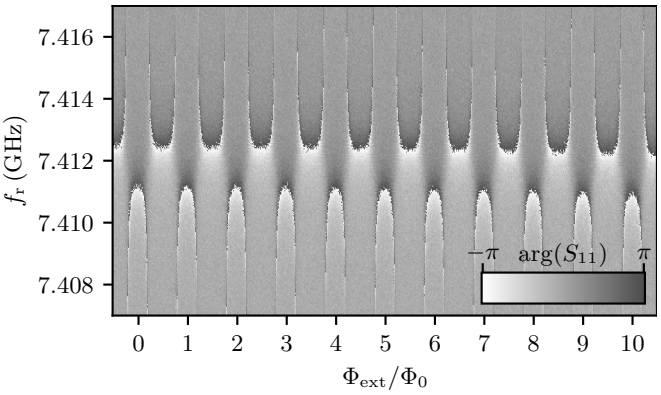

FIG. S2. **Extended flux sweep of the readout resonator up to $\Phi_{\rm ext}/\Phi_0 = 10$.** The strict periodicity is superimposed by a $\approx$ 200 kHz parabolic frequency shift due to screening currents in the antenna. The measurement was performed in a previous cooldown compared to Fig. 2a, which is why the resonance frequency is 2.5 MHz higher.

I. SAMPLE HOLDER

In Fig. S1 we show the copper sample holder used for cryogenic microwave reflection measurements (cf. also Ref. [1]). The 3 mm inner diameter of the waveguide corresponds to a cut-off frequency of 60 GHz. The microwave coupling of the readout resonator is given by evanescent waves from the central pin of the coaxial cable connected to the waveguide.

II. QUBIT-RESONATOR AVOIDED CROSSINGS

The signature of a gralmonium device operating in the desired frequency range and coupled to the readout resonator is the measurement of qubit-resonator avoided level crossings (cf. Fig. 2a), periodic in flux. In Fig. S2 we present measurements of the qubit-resonator anti-crossings for the main text device, extending over 10 Φ_0 periods. The 200 kHz frequency shift observable between the anti-crossing patterns at $\Phi_{\rm ext}/\Phi_0 = 0$ and $\Phi_{\rm ext}/\Phi_0 = 10$, is due to the frequency dependence of the grAl antenna as a function of out-of-plane field, consistent with Ref. [1].

The $E_{\rm J}/E_{\rm C}$ ratio for the grAl nano-junction is highly sensitive to its width, which can lead to very different spectra for nominally identically fabricated devices, simply due to lithography variability. A rapid method to select working devices is to measure their field dependence. As an example, in Fig. S3 we compare three devices with nominally identical design for the gralmonium and nano-junction, fabricated in the same evaporation on the same chip and measured in the same cooldown. The flux sweeps reveal three different junction regimes. The device presented in Fig. S3a shows a 1 MHz shift but no qubit-resonator avoided level crossings. This can be explained by the fact that the ratio $E_{\rm J}/E_{\rm C}$ for this nano-junction is much larger than unity, and quantum fluctuations of the phase are suppressed. In this case the flux bias induces persistent currents in the device loop, responsible for the 1 MHz frequency shift (which is much larger than the frequency dependence vs. field of the bare antenna, as shown in Fig. S3c). The corresponding SEM micrograph of the nano-junction confirms its relatively large size, with $\varepsilon \approx 50$ nm. The flux sweep presented in Fig. S3b shows qubit-resonator avoided level crossings similar to Fig. 2a, and the corresponding SEM micrograph confirms the smaller width of the grAl nano-junction of this device compared to Fig. S3a. In Fig. S3c we show the measurement of a device where the grAl nano-junction is interrupted. As expected for this flux range, we do not observe a change in the frequency of the readout resonator.

Based on SEM imaging of 53 devices, we find 22% of nano-junctions to be in the regime shown in Fig. S3b, i.e. connected junctions with $\varepsilon \leq 25$ nm. These statistics can be improved by using thinner resist layers and by replacing the chromium anti-static coating for e-beam writing (cf. Methods) with aluminum, which yields reduced roughness. Thanks to the single-layer circuit design, etching is a tantalizing alternative to lift-off fabrication with the added benefit of using sub 10 nm resolution negative e-beam resists. In addition to improving the lithography reliability, first experiments indicate that

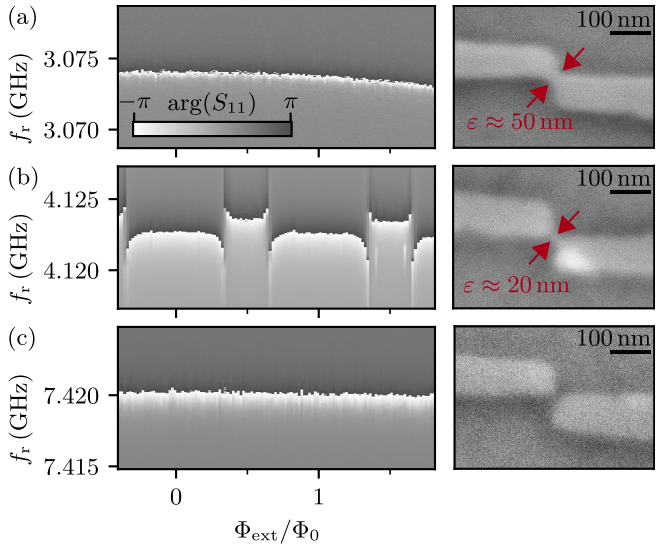

FIG. S3. **Comparison of grAl nano-junction regimes.** The left column shows the phase of the reflection coefficient measured versus external flux for three different samples with nominally identical gralmonium and nano-junction design. The right column depicts the corresponding SEM image of the grAl nano-junction, taken after the cooldown. **(a)** The resonator frequency slightly decreases with increasing external flux due to a too wide nano-junction ($\varepsilon \approx 50\,\mathrm{nm}$) and resulting screening currents in the loop. **(b)** The flux sweep shows periodic avoided level-crossings, which are the signature of a functioning gralmonium attached to the resonator. The nonlinear element is in the same regime of $\varepsilon \approx 20\,\mathrm{nm}$ as the main sample (Fig. 1). **(c)** The resonator frequency is constant in this field range because the nano-junction is interrupted.

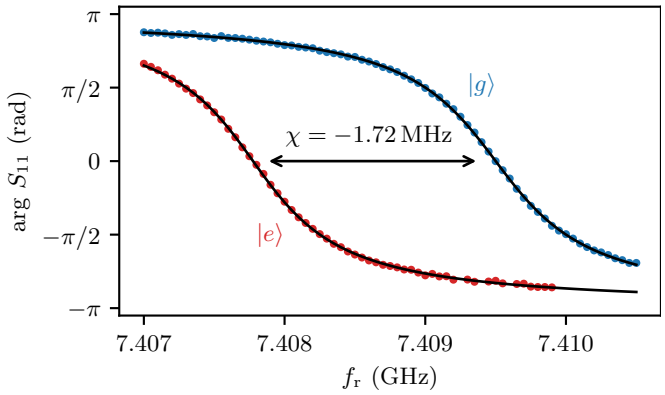

FIG. S4. **Dressed resonator phase responses for qubit in $|g\rangle$ (blue) and $|e\rangle$ (red).** The data is extracted from IQ histograms similar to the one shown in Fig. 2c with a $\pi/2$ qubit pulse applied before the readout pulse, in order to balance the populations of the qubit states. By fitting the phase responses, we extract a dispersive shift of $\chi/2\pi = -1.72\,\mathrm{MHz}$ and a resonator linewidth of $\kappa/2\pi = 1.00\,\mathrm{MHz}$.

post-processing samples with wet-etching or annealing can tune nano-junctions closer to a desired E_J regime. Moreover, we expect that nano-junctions as shown in Fig. S3a might also lead to working gralmonium devices for sufficiently large sheet resistivity, as long as the grAl film remains superconducting.

III. EXTRACTION OF DISPERSIVE SHIFT

In Fig. S4, we show the method to extract the dispersive shift between the dressed resonator responses for the qubit in $|g\rangle$ and $|e\rangle$. The regime of $|\chi| > \kappa$ enables qubit readout with maximum 180° phase separation (Fig. 2).

IV. SINUSOIDAL CURRENT PHASE RELATION OF THE NANO-JUNCTION

In the following, we quantify how accurately the standard fluxonium Hamiltonian Eq. 1 with sinusoidal nano-junction current-phase relation (CφR) describes the measured gralmonium spectrum shown in Fig. 2 in the main text. To do so, in addition to numerically diagonalizing Eq. 1 using the pure sinusoidal CφR we also consider two other CφRs increasingly deviating from a pure sine. We construct these CφRs by adding higher order terms $\sin(n\varphi)\,(n > 1)$ [2]. The diagonalization is performed using a straightforward extension of the same numerical method used in the main text [3]. We fit the model to the experimental data for each CφR individually. For the purely sinusoidal case it is feasible to also include the coupling to the readout resonator in the model in order to describe the avoided-level crossings between qubit and resonator, while for the non-sinusoidal CφRs this task becomes computationally intensive.

The CφRs used for the analysis, their corresponding energy phase relations and the comparison between model and measurement are shown in Fig. S5. Remarkably, the standard sinusoidal CφR matches the data to within $\pm 2\,\mathrm{MHz}$. In contrast, the models with higher order contributions systematically deviate from the data by an order of magnitude. Based on the spread of the measured values for the $|g\rangle \rightarrow |e\rangle$ frequencies, we cannot rule out higher order Josephson harmonics with a relative contribution smaller than 5 %.

V. ZERO FLUX COHERENCE

In Fig. S6 we present energy relaxation and coherence measurements of the $|g\rangle \rightarrow |e\rangle$ transition performed at zero flux bias. Notably, the transition is not plasmon-like in our device, which is illustrated in Fig. S7 by the energy potential and wavefunctions.

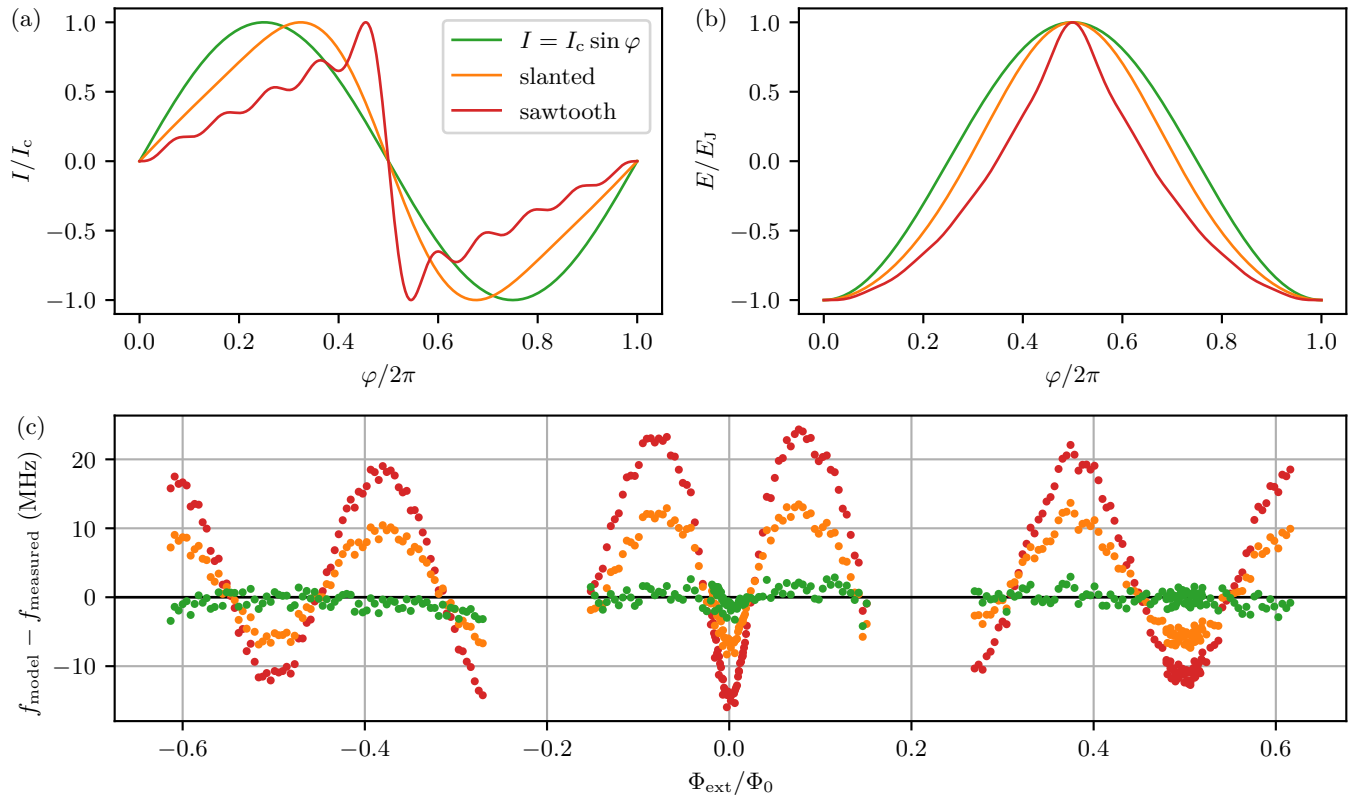

FIG. S5. **Comparison between the measured spectrum and the fluxonium Hamiltonian.** **(a)** Current phase relations (CφRs) used for modeling. In addition to the standard SIS JJ sinusoidal CφR, $I = I_c \sin\varphi$ (green), we consider two other models containing higher order Josephson harmonics [2]: a slanted CφR, $I = I_c(\sin\varphi - 0.25\sin 2\varphi + 0.05\sin 3\varphi)$ (orange), and a sawtooth-like CφR, $I = I_c \sum_{n=1}^{10}(-1)^{(n+1)}\sin(n\varphi)/n$ (red). **(b)** Energy phase relations corresponding to the CφRs in (a). In **(c)** we plot the difference between the measured eigenfrequencies $f_{measured}$ for the $|g\rangle \rightarrow |e\rangle$ transition (cf. Fig. 2) and the numerical diagonalization f_{model} using Hamiltonian Eq. 1, where the Josephson term is given by the energy phase relations plotted in (b). We exclude a ± 1 GHz interval in the vicinity of the avoided level crossing with the resonator ($|\Phi_{ext}/\Phi_0| \approx 0.2$). Notably, the standard sinusoidal CφR used in the main text (green) shows no deviations within ± 2 MHz, which is the resolution of the measurement. In contrast, the non-sinusoidal CφRs (orange and red corresponding to (b)) show order of magnitude larger and systematic deviations. Based on this measurement, we place an upper bound of 5 % for higher harmonics contributions in the CφR of the nano-junction.

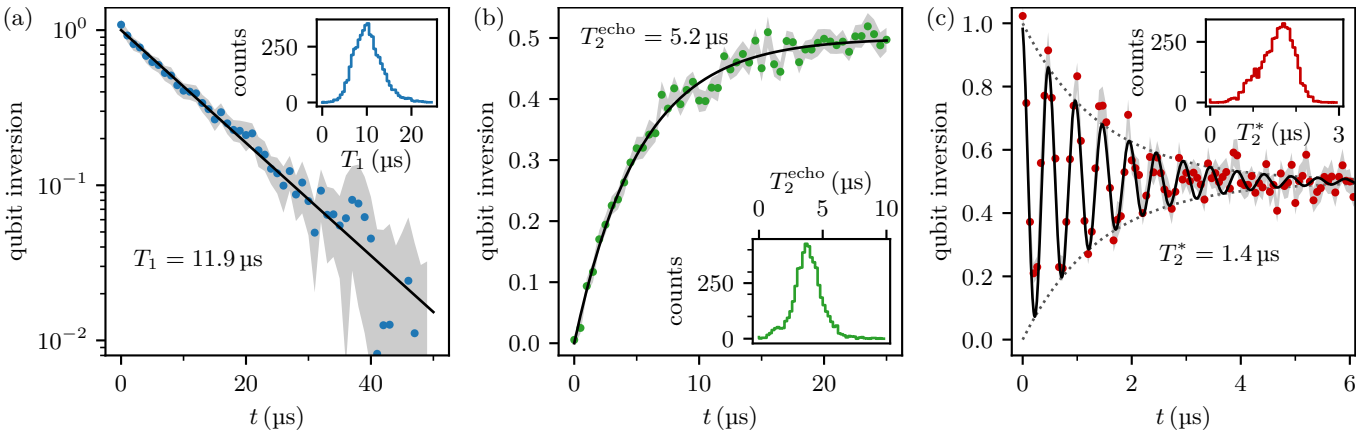

FIG. S6. **Time domain characterization at zero flux.** **(a)** Free decay energy relaxation and **(b)** spin Hahn echo experiment with exponential fits (black lines). While the average T_1 is comparable to half flux, T_2^{echo} is a factor of 2 lower. **(c)** Ramsey fringes with a nominal detuning of 2 MHz. In contrast to half flux, we do not observe a revival of Ramsey fringes at zero flux and the fit (black line) consists of a single sine wave with exponential envelope (dotted lines).

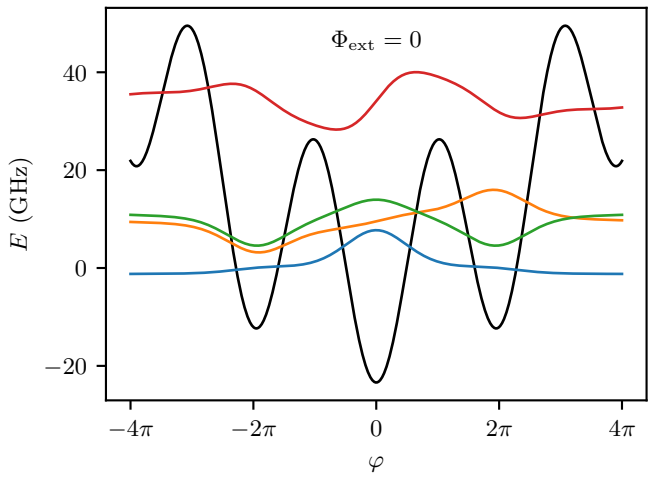

FIG. S7. **Gralmonium energy potential (black) and wavefunctions (colored) at zero flux bias.** We plot the first four wavefunctions, vertically offset by their eigenenergy. Note that all wavefunctions are significantly delocalized over three potential wells and, for this reason, the $|g\rangle \rightarrow |e\rangle$ transition is not plasmon-like.

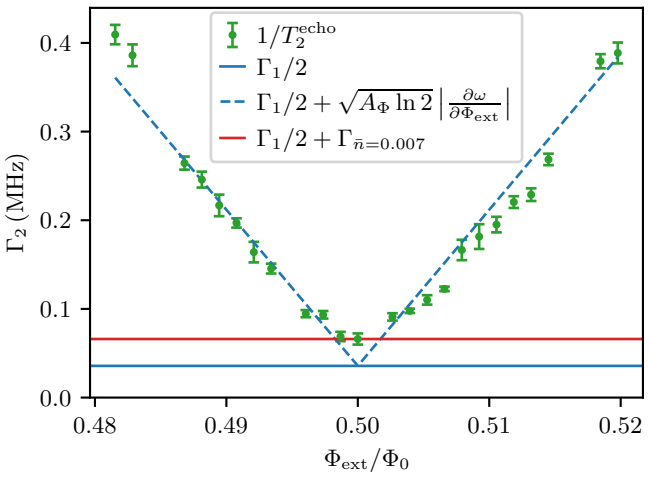

FIG. S8. **Analysis of gralmonium decoherence around half flux bias.** Green markers show the echo decoherence rate $\Gamma_2^{\rm echo} = 1/T_2^{\rm echo}$ based on the same data as shown in Fig. 3c in the main text. The markers and errorbars represent the mean and standard error of the mean of decoherence rates extracted in 5 repeated flux sweeps. The contribution from energy relaxation $\Gamma_1/2$ is indicated by the blue horizontal line. From the linear increase of $\Gamma_2^{\rm echo}$ we extract a flux noise amplitude of $A_\Phi = 30\,\mu\Phi_0$ (dashed blue lines). The residual decoherence exactly at half flux is consistent with shot noise corresponding to an average thermal population of $\bar{n} \approx 0.007$ in the readout resonator, but could also stem from higher order flux noise.

VI. GRALMONIUM DECOHERENCE AROUND HALF FLUX

Here, we discuss in more detail the $T_2^{\rm echo}$ data in the vicinity of $\Phi_{\rm ext}/\Phi_0 = 0.5$ shown in Fig. 3c in the main text. The corresponding decoherence rate $\Gamma_2^{\rm echo} = 1/T_2^{\rm echo}$ is plotted in Fig. S8 (green markers). The decoherence budget consists of energy relaxation $\Gamma_1/2$, flux noise $\Gamma_\Phi(\Phi_{\rm ext})$, photon shot noise due to stray photons in the resonator $\Gamma_{\bar{n}}$ and critical current noise in the nanojunction and superinductor Γ_{I_c}:

$$\Gamma_2^{\rm echo} = \frac{\Gamma_1}{2} + \Gamma_\Phi(\Phi_{\rm ext}) + \Gamma_{\bar{n}} + \Gamma_{I_c}\,. \tag{1}$$

Energy relaxation vs. external flux is flat in the measured range (cf. Fig. 3c) with an average $T_1 = \Gamma_1^{-1} = 14\,\mu$s, which corresponds to a constant contribution to decoherence $\Gamma_1/2$ indicated by the horizontal blue line in Fig. S8. We observe a linear increase of $\Gamma_2^{\rm echo}$ around half flux bias and from the slope we extract a $1/f$ flux noise amplitude of $A_\Phi = 30\,\mu\Phi_0$. Note that due to limited resolution and SNR of the echo measurements we cannot exclude an additional, flux dependent, Gaussian component in the decay curves, which is why we use an exponential to consistently fit the entire data set. Exactly at half flux, $\Gamma_2^{\rm echo}$ remains approximately a factor of 2 above the T_1-limit $\Gamma_1/2$. This residual dephasing could be either due to higher order flux noise contributions or photon shot noise. The dephasing due to photon shot noise in the low photon limit is given by [4, 5]

$$\Gamma_{\bar{n}} = \frac{\bar{n}\kappa\chi^2}{\kappa^2 + \chi^2}\,. \tag{2}$$

Based on the independently measured values of χ and κ (cf. App. III), the residual dephasing rate corresponds to a thermal population of $\bar{n} \approx 0.007$, consistent with literature (see e.g. [4]). Finally, the critical current noise is the only contribution which can be filtered efficiently by the echo sequence, and is likely explaining the factor of 3 higher $T_2^{\rm echo}$ compared to Ramsey decay time T_2^* at half flux. The echo sequence filters noise on timescales between 10 µs (the filter function cut-off) and ms which is already captured by the two frequency fit for the Ramsey measurement.

VII. QUANTUM JUMP ANALYSIS

In Fig. S9 we analyze the contiguously measured reflection coefficient of the readout resonator as a function of time. The measured data is the same as histogrammed in Fig. 2c. We rotated the IQ plane such that the qubit state information is encoded in the in-phase quadrature I. From a double gaussian fit to the marginal distribution along the I quadrature, we extract the means $\mu_{\rm g,e} \approx \pm 3.0\sqrt{\rm photon}$ and standard deviations $\sigma_{\rm g,e} \approx 1.0\sqrt{\rm photon}$ for the qubit states. To assign the qubit state to the demodulated contiguous data, we use a two-point latching filter, which declares a change in the qubit state when the in-phase value I enters the $\mu \pm 2\sigma$ band (Fig. S9a) centered on the other

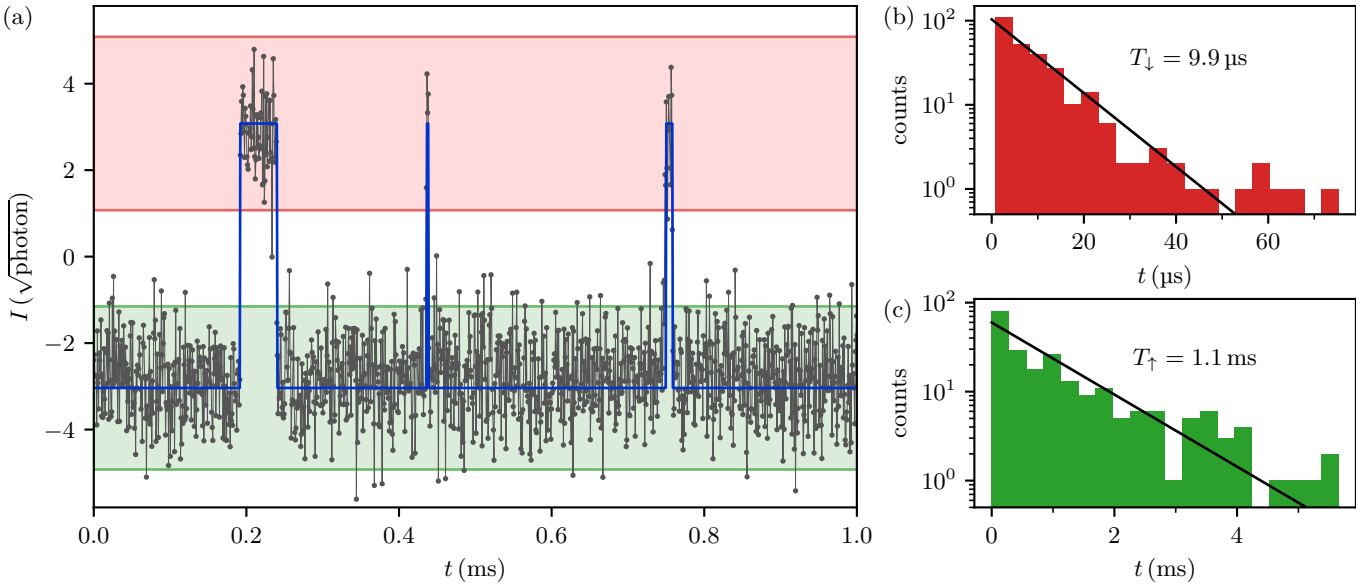

FIG. S9. **Quantum jump measurement at half-flux bias point of the gralmonium. (a)** Example time trace of the in-phase component I of the readout resonator reflection coefficient (black connected markers). We apply a continuous readout tone, populating the resonator with $\bar{n} \approx 10$ photons, and we demodulate contiguous windows of $\tau = 784\,ns$. The qubit state is assigned using a latching filter (blue line) based on the $\pm 2\sigma$ bands (green and red for $|g\rangle$ and $|e\rangle$, respectively) around the mean values of the qubit states. The corresponding IQ histogram of the demodulated data for a total measurement time of 500 ms is shown in Fig. 2c. In **(b)** and **(c)** we histogram the durations spent by the qubit in the excited and ground state, respectively. Maximum likelihood exponential fits yield the average relaxation and excitation times $T_\downarrow = 9.9\,\mu s$ and $T_\uparrow = 1.1\,ms$, respectively.

qubit state. The extracted population of the excited state corresponds to an effective qubit temperature of 37 mK. Moreover, by histogramming the lifetime of the states (Fig. S9b,c), we find the energy relaxation during readout $T_1 = (T_\downarrow^{-1} + T_\uparrow^{-1})^{-1} = 9.8\,\mu s$, practically unchanged from the free decay value (Fig. 3a).

VIII. EVIDENCE OF E_J TOGGLING IN THE GRALMONIUM SPECTRUM VS. FLUX

As discussed in the main text and in Fig. 3, the gralmonium frequency toggles even when kept at cryogenic temperatures. This toggling is also visible in continuous wave spectroscopy versus flux when the trace averaging time is comparable to the respective timescale of the toggling. In the half flux spectroscopy discussed in the main text (Fig. 2b inset), the toggling on minutes timescale is visible as jumps in the qubit frequency every few traces. In Fig. S10, we show spectroscopy in a previous cooldown without a parametric amplifier, where the averaging time per trace is about one order of magnitude longer. Therefore, the toggling on minutes timescale is imprinted on the spectroscopy data as distinct qubit lines associated to the qubit transitions. In contrast to the jumps between traces in Fig. 2b, the distinct qubit lines are visible in Fig. S10 within the same trace. The observation of two qubit frequencies across the entire flux range rules out a transverse coupling to parasitic two level systems (TLSs) residing at fixed frequency. Indeed, the two qubit lines are captured by two numerical fits to the fluxonium Hamiltonian, which differ only in the value of the Josephson energy E_J. Notably, the two-E_J-model correctly predicts the merging of the two frequencies at $\Phi_{ext}/\Phi_0 \approx 0.08$ (Fig. S10b), as well as their frequency inversion between zero and half-flux biases.

IX. POWER SPECTRAL DENSITY

For a quantitative analysis of the toggling of the qubit frequency on minutes timescale, we calculate the power spectral density

$$S(f) = \mathcal{F}^2(f_{01}) \cdot 2T\,, \tag{3}$$

where $\mathcal{F}(f_{01})$ is the normalized discrete Fourier transform and T is the total measurement duration. From double-frequency fits (cf. Fig. 3d) to 400 contiguous Ramsey measurements, we extract a time series of the Ramsey frequency f_{Ramsey} and the beating frequency f_{beating} with a total duration $T = 832\,s$. Figure S11 shows the power spectrum for f_{Ramsey} (blue markers) and f_{beating} (green markers) averaged over 85 traces. The power spectrum of f_{Ramsey} follows a Lorentzian shape characteristic for random telegraphic noise (RTN),

$$S(f) = \frac{b\Gamma_{\text{RTN}}^2}{f^2 + \Gamma_{\text{RTN}}^2} + S_0\,, \tag{4}$$

where Γ_{RTN} is the switching rate, b the amplitude and S_0 the frequency independent white noise floor. A fit to

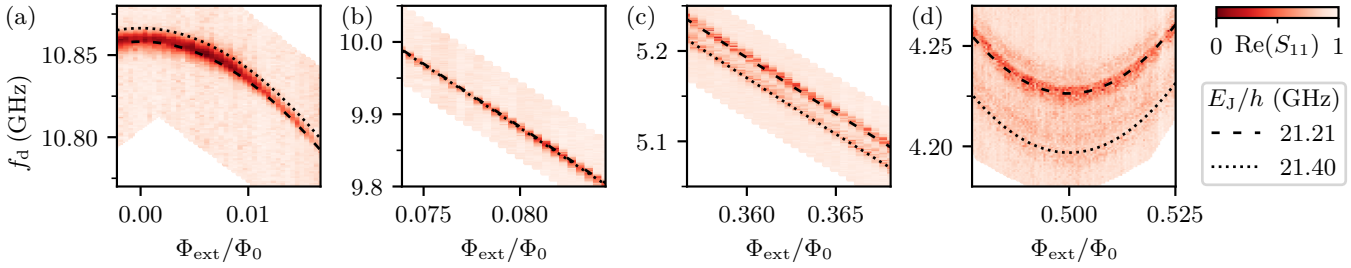

FIG. S10. **Evidence of E_J toggling in the gralmonium spectrum vs. flux.** The panels show spectroscopy of the same gralmonium as in Fig. 2, but in a previous cooldown (#3) without the use of a parametric amplifier. Each trace is averaged over 50 s and contains 100 points. The color scale corresponds to the in-phase component of the single-port reflection coefficient S_{11}, with the minimum and maximum values rescaled to the $0-1$ interval for clarity. Two dominant qubit frequencies are visible across the entire flux range and can be fitted (dashed and dotted line) with identical circuit parameters except for the values of the nano-junction E_J, which differ by 190 MHz. Close to zero flux (**a**) the difference between the two spectra is 7.4 MHz. As expected from the model, the lines cross at $\Phi_{ext}/\Phi_0 \approx 0.08$ (**b**) and they are again visibly separated towards half-flux (**c**). The largest splitting (30 MHz) occurs at half-flux (**d**), where additional lines also become visible.

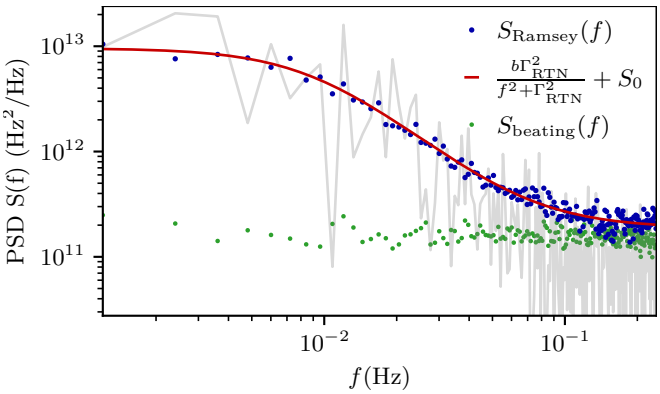

FIG. S11. **Power spectral density $S(f)$ of the gralmonium frequency on the minutes timescale.** The power spectral density is calculated from a timetrace of 400 measurements of the gralmonium frequency extracted from contiguous Ramsey experiments, with a total duration of 832 s (example in light gray). This sequence is repeated 85 times and the blue markers show the averaged power spectrum. The power spectrum $S_{Ramsey}(f)$ follows a Lorentzian shape at low frequencies, corresponding to random telegraphic noise (RTN). A fit (red line) reveals the switching rate $\Gamma_{RTN} = 9.4$ mHz, amplitude $b = 1.89 \times 10^{13}$ Hz^2/Hz and white noise floor of $S_0 = 3.73 \times 10^{11}$ Hz^2/Hz. For comparison, the power spectrum of the beating frequency $f_{beating}$ (cf. Fig. 3d) obtained from the same measurements only consists of a white noise component (cf. green markers).

$S_{Ramsey}(f)$ (red line) reveals a switching rate of $\Gamma_{RTN} = 9.4$ mHz. In contrast, the power spectrum of the beating frequency $f_{beating}$ is frequency independent.

X. ADDITIONAL GRALMONIUM SPECTRA

The gralmonium sample discussed in the main text was measured in 6 consecutive cooldowns (Fig. S12), revealing significantly different spectra. From fits (black lines) to the fluxonium Hamiltonian (Eq. 1) we identify the nano-junction E_J as the parameter which changes the most between cooldowns. The total gralmonium capacitance $C_\Sigma = C_q + C_J$ also changes and appears to be correlated with E_J, however, it is bounded by the finger capacitance $C_q \approx 0.8$ fF. Therefore, the gralmonium charging energy is limited to values below $E_C^\Sigma \leq E_C^q \approx 24$ GHz.

Including the sample characterized in the main text, we measured the spectra of 20 gralmonium devices across 11 wafers and all data is consistent with the standard fluxonium Hamiltonian Eq. 1. In Fig. S13 we show the spectra and fit parameters of three selected devices with the same circuit design as in Fig. 1. The spread of the Josephson energy across devices, 7–40 GHz, is similar to variations of individual nano-junctions in successive cooldowns (8–27 GHz, cf. Fig. S12).

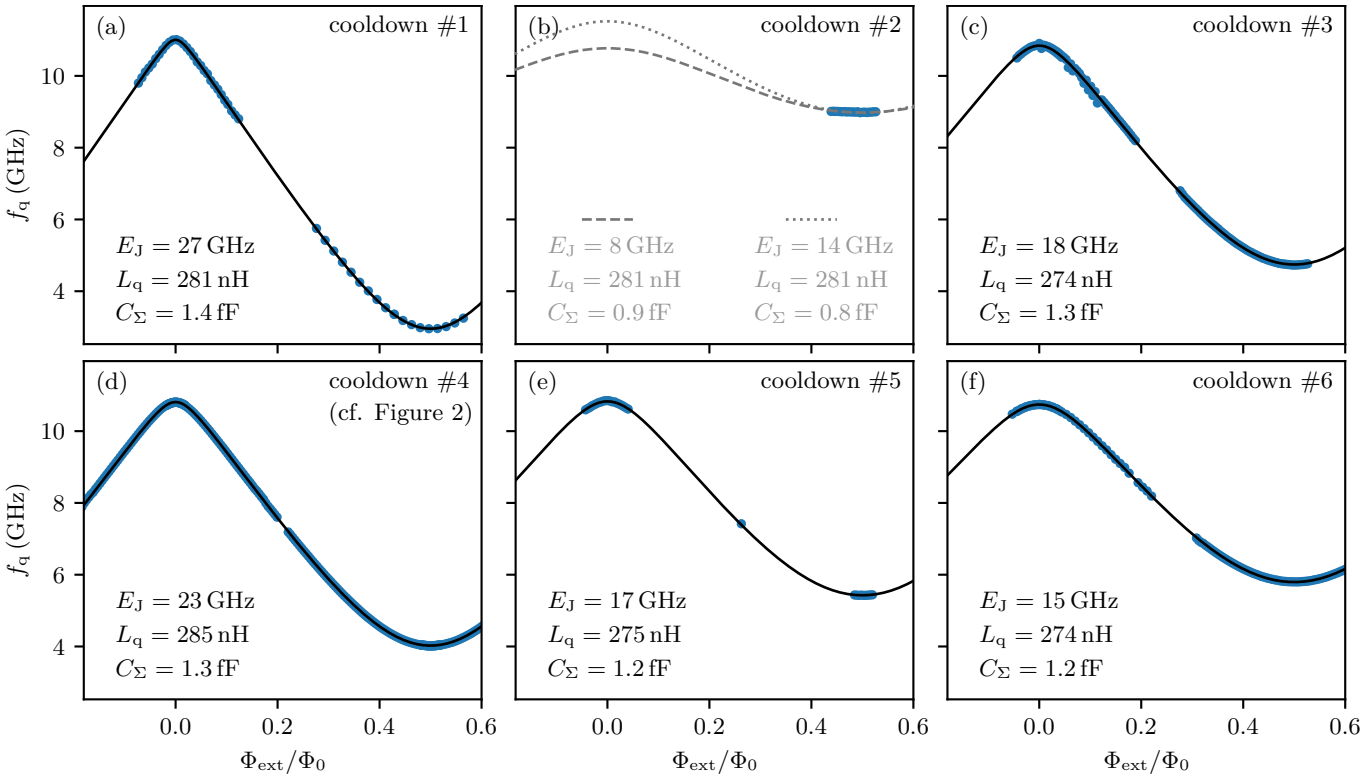

FIG. S12. **Spectra and fit parameters in consecutive cooldowns of the main sample.** The blue markers are extracted from spectroscopy of the $|g\rangle \rightarrow |e\rangle$ transition and the black lines show numerical fits of Eq. 1 to the data. The spectrum undergoes significant changes between cooldowns, particularly visible at half-flux. The corresponding changes in half-flux frequency and E_J are summarized in Fig. 3e. A comparison of the fit parameters reveals relatively large changes in E_J and moderate changes in C_Σ. In contrast, the inductance L_q remains constant within few percent. For the second cooldown (panel **(b)**) only data around half-flux was taken, making an unambiguous fit difficult. Instead, we show two plausible parameter sets by fixing L_q to the value of the previous cooldown and C_Σ around the lower bound $C_q \gtrsim 0.8\,\mathrm{fF}$ expected from the finger capacitance and observed in other samples (cf. Fig. S13a).

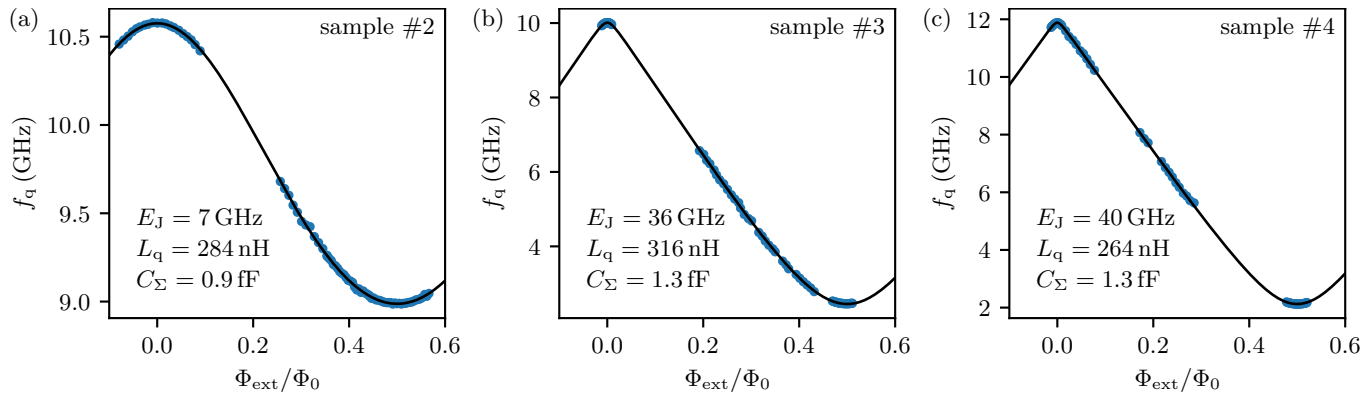

FIG. S13. **Spectra and parameters of additional gralmonium samples**. The blue markers are extracted from spectroscopy of the $|g\rangle \rightarrow |e\rangle$ transition and the black lines show numerical fits of Eq. 1 to the data. **(a)** The Josephson energy of some grAl nano-junctions is small enough to lift the entire spectrum of the first transition to the 10 GHz range. Samples **(b)** and **(c)** feature similar parameters as the gralmonium in Fig. 2.

[1] K. Borisov, D. Rieger, P. Winkel, F. Henriques, F. Valenti, A. Ionita, M. Wessbecher, M. Spiecker, D. Gusenkova, I. M. Pop, and W. Wernsdorfer, Superconducting granular aluminum resonators resilient to magnetic fields up to 1 Tesla, Appl. Phys. Lett. **117**, 120502 (2020).

[2] A. A. Golubov, M. Y. Kupriyanov, and E. Il'ichev, The current-phase relation in Josephson junctions, Rev. Mod. Phys. **76**, 411 (2004).

[3] W. C. Smith, A. Kou, U. Vool, I. M. Pop, L. Frunzio, R. J. Schoelkopf, and M. H. Devoret, Quantization of inductively shunted superconducting circuits, Phys. Rev. B **94**, 144507 (2016).

[4] G. Zhang, Y. Liu, J. J. Raftery, and A. A. Houck, Suppression of photon shot noise dephasing in a tunable coupling superconducting qubit, npj Quantum Information **3**, 1 (2017).

[5] A. A. Clerk and D. W. Utami, Using a qubit to measure photon-number statistics of a driven thermal oscillator, Phys. Rev. A **75**, 042302 (2007).